Author for correspondence:
David Robert Grimes
e-mail: d.r.grimes@qub.ac.uk or davidrobert.grimes@oncology.ox.ac.uk

Oxygen diffusion in ellipsoidal tumour spheroids

David Robert Grimes[1,2] and Frederick J. Currell[3]

[1]Centre for Advanced and Interdisciplinary Radiation Research (CAIRR) School of Mathematics and Physics, Queen's University Belfast, Belfast BT7 1NN, UK
[2]Cancer Research UK/MRC Oxford Institute for Radiation Oncology, Gray Laboratory, University of Oxford, Old Road Campus Research Building, Off Roosevelt Drive, Oxford OX3 7DQ, UK
[3]The Dalton Cumbrian Facility and School of Chemistry, University of Manchester, Westlakes Science and Technology Park, Moor Row, Whitehaven CA24 3HA, UK

[iD] DRG, 0000-0003-3140-3278

Oxygen plays a central role in cellular metabolism, in both healthy and tumour tissue. The presence and concentration of molecular oxygen in tumours has a substantial effect on both radiotherapy response and tumour evolution, and as a result the oxygen micro-environment is an area of intense research interest. Multi-cellular tumour spheroids closely mimic real avascular tumours, and in particular they exhibit physiologically relevant heterogeneous oxygen distribution. This property has made them a vital part of *in vitro* experimentation. For ideal spheroids, their heterogeneous oxygen distributions can be predicted from theory, allowing determination of cellular oxygen consumption rate (OCR) and anoxic extent. However, experimental tumour spheroids often depart markedly from perfect sphericity. There has been little consideration of this reality. To date, the question of how far an ellipsoid can diverge from perfect sphericity before spherical assumptions break down remains unanswered. In this work, we derive equations governing oxygen distribution (and, more generally, nutrient and drug distribution) in both prolate and oblate tumour ellipsoids, and quantify the theoretical limits of the assumption that the spheroid is a perfect sphere. Results of this analysis yield new methods for quantifying OCR in ellipsoidal spheroids, and how this can be applied to markedly increase experimental throughput and quality.

1. Introduction

Oxygen plays a seminal role in cancer treatment and patient prognosis. The presence of molecular oxygen in a tumour markedly increases radio-sensitivity, with well-oxygenated regions responding to radiotherapy by up to a factor of 3 relative to anoxic sub-volumes [1,2]. This oxygen enhancement ratio is also seen in emerging modalities such as proton therapy [3,4], raising the tantalizing prospect of dose painting, where dose is selectively boosted to hypoxic regions to boost therapy response [5]. The basic idea underpinning dose painting has been discussed for over a decade, but application has been hampered by difficulty in non-invasive hypoxia imaging. Methods such as F-MISO PET (fluoromisonidazole positron emission tomography) have a maximum resolution in the millimetre regime, while oxygenation varies over a micrometre scale. As a consequence, mathematical modelling is vital for bridging the resolution gap [6].

Aside from therapeutic considerations, oxygen has a marked impact on patient prognosis. The pioneering work of Gray and colleagues in the early 1950s established that tumour oxygen concentration was correlated with prognosis, and extensive hypoxia was a negative prognostic marker [7]. This finding has been well replicated to present day [8–10] and is not solely due to hypoxia-induced treatment resistance. Under severe hypoxia, tumour cells can respond

to such pressure by activating oxygen-sensitive signalling pathways [11,12]. Current biological thinking suggests that these signalling pathways act to alter gene expression to promote cell survival under adverse conditions. Hypoxia is also a major driver of angiogenesis, giving rise to new routes for cells to travel along [13,14], endowed with the ability to metastasize [15].

The extraordinary importance of oxygen in cancer treatment and evolution has made it an important avenue of study, with an urgent need for further research. Despite the fundamental importance of molecular oxygen in tumours, investigations have been complicated by the significant experimental difficulty in ascertaining oxygen concentration *in situ* [6]. Real tumours have highly heterogeneous oxygen supply and complex tortured vasculature, and even well-oxygenated regions are frequently inter-spaced with pockets of anoxia [14,16]. Standard two-dimensional monolayers of cells are not an ideal experimental model, typically exhibiting an unrealistically homogeneous oxygen contribution. There is however a more realistic experimental option in the form of tumour spheroids. These clusters of cancer cells grow in approximately spherical three-dimensional aggregates, and exhibit signalling and metabolic profiles more similar to real tumours than is observed in monolayer approaches [17–19].

Like monolayers, spheroids are relatively easy to culture, and growing interest has seen them used for a variety of purposes, including radiobiological application as a means to test fractionation [20–23], as a model for drug delivery [24–28], for investigation of the stem-cell hypothesis [29] and for exploring FDG-PET (fludeoxyglucose positron emission tomography) dynamics [30] for hypoxia in solid tumours. Crucially, the non-homogeneous oxygen distributions in tumour spheroids have been well studied [31–33]. Research to date shows that cellular oxygen consumption rate (OCR) has a known influence on the oxygen concentration throughout a spheroid, and directly influences the extent of central anoxia and the viable rim thickness by known mathematical relationships [32]; thus measuring these aspects allows an experimenter to determine OCR with relative ease compared with other methods [28].

Such methods and the underlying theory are exceptionally important to understanding the factors that influence tumour oxygen distribution, yet all these methods rely on an implicit assumption of perfect sphericity. There is a clear rationale behind this, as symmetry considerations simplify the problem greatly. Yet in experimental conditions, imperfect spheroids are common, frequently growing as extended ellipsoids. When the eccentricity of these shapes is extreme, an experimenter may reasonably choose to discard them from analysis. But this prompts a question: quite how extreme do such deformations have to be before a spherical assumption breaks down? Presumably small departures from sphericity should not impact analysis, whereas highly eccentric ellipsoids could reasonably be presumed to violate the underlying theoretical assumptions. The question of how such eccentricities might skew analysis of spheroids, and how trustworthy results of such analysis might be, has not yet been considered in the literature, despite its obvious practical importance.

These questions are as of yet unanswered, and are of paramount importance given the growing adoption of spheroids for cancer research, and their utility in estimating OCR [31,32]. Knowing the acceptable limits of eccentricity for spheroid analysis would be of considerable benefit to experimenters, providing error estimates and limits of reliability. A full analytic expression for 'ellipsoidals' (analogous to the spherical case) would also be of substantial benefit, allowing the analysis of eccentric shapes and potentially increasing experimental throughput. In this work, we seek to address these issues by deriving an expression for oxygen diffusion in both prolate and oblate geometries. This is contrasted to the spherical case to determine the limits of validity for experimental data, and the implications of this are discussed. A schematic of this is depicted in figure 1.

1.1. Spheroids and ellipsoids

The general equation of an ellipsoid is given by

$$\frac{x^2}{a^2} + \frac{y^2}{b^2} + \frac{z^2}{c^2} = 1, \qquad (1.1)$$

where a, b and c are the major axes' lengths. For an ellipsoid with azimuthal symmetry, $a = b$. When all axes are equal ($a = b = c$), the result is a perfect sphere. To date, this is the only case which has been well studied from a theoretical standpoint [31–33]. While the mathematical treatments to date have assumed spheroids are perfect spheres, the nomenclature 'spheroid' still applies to the more general case, including prolate and oblate spheroids. In this work, we broaden the mathematical framework to be applicable to ellipsoids without full spherical symmetry, which are namely

(1) *Prolate spheroids*. In the case where $c > a$, the resulting ellipsoid is an ellipse rotated around its major axis, the line joining its foci. This yields a rugby ball-type shape.
(2) *Oblate spheroids*. Where $a > c$, an oblate spheroid results, equivalent to an ellipse rotated around its minor axes. The resulting shape is discus-like.

Examples of these ellipsoids are shown in figure 2. To avoid confusion, we use the term spheroid to refer to an ellipsoidal collection of cells, although we do not limit this to perfect spheres, qualifying with terms 'prolate' or 'oblate' as appropriate. We use the term ellipsoid to refer to surfaces of iso-concentration of oxygen.

2. Model derivation

The full mathematical derivation for oxygen partial pressure in prolate and oblate spheroids is rather involved, and here we shall confine ourselves to stating results with a cursory outline of how they are derived. A full mathematical outline is provided in the electronic supplementary material, appendix, S1. Essentially, we are concerned with solving a steady-state reaction–diffusion problem for oxygen field P of the form

$$D\nabla^2 P = a\Omega, \qquad (2.1)$$

where D is the oxygen diffusion constant in water (typically $D = 2 \times 10^{-9} \, \text{m}^2 \, \text{s}^{-1}$) and $a\Omega$ is the oxygen consumption rate in mmHg s^{-1}. This must be solved subject to two crucial boundary conditions, namely that the surface flux and
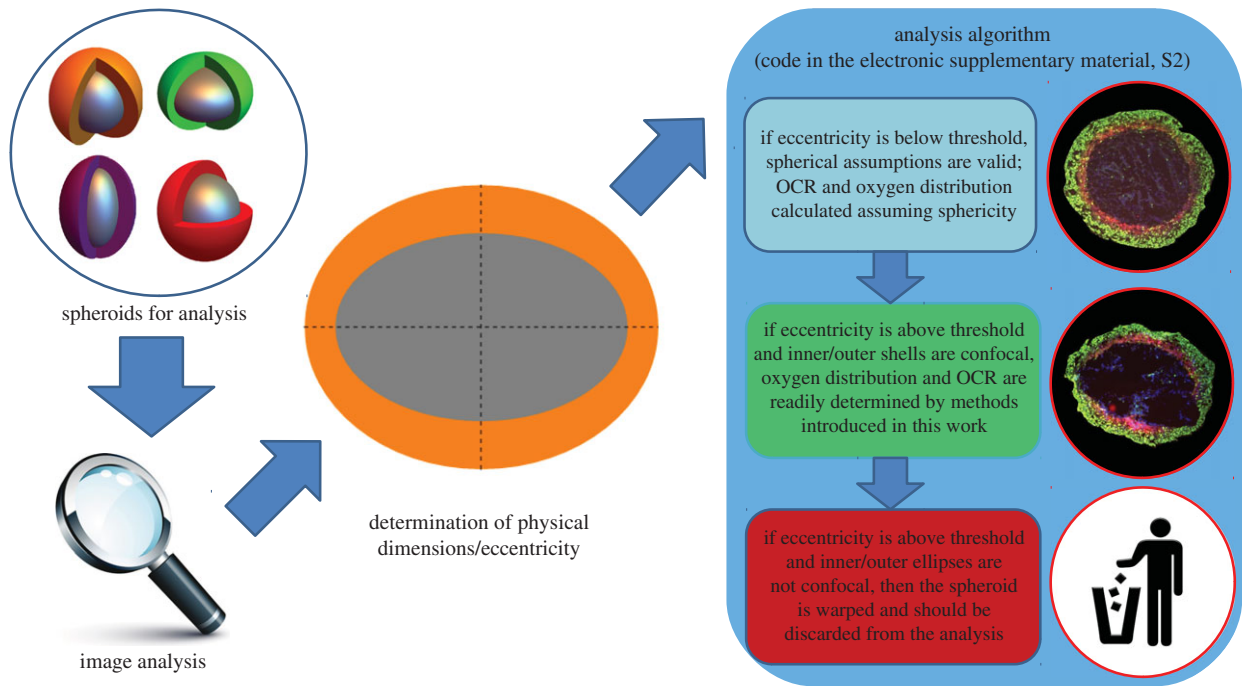
Figure 1. Schematic analysis in this work. Below a calculated threshold for eccentricity, spheroids can be treated as having perfect sphericity without introducing unacceptable error, and their OCR and oxygen distribution established by previously published methods [32]. At greater eccentricities, however, a spherical assumption is no longer valid. If the inner and outer sections are concentric ellipses, these can be analysed by the methods outlined in this work to ascertain OCR and oxygen distribution. If eccentricity is higher than a threshold value, and inner and outer ellipses are not concentric, this suggests the spheroid is severely warped or the section is off the central axis, and should be discarded from analysis. See text for details. (Online version in colour.)
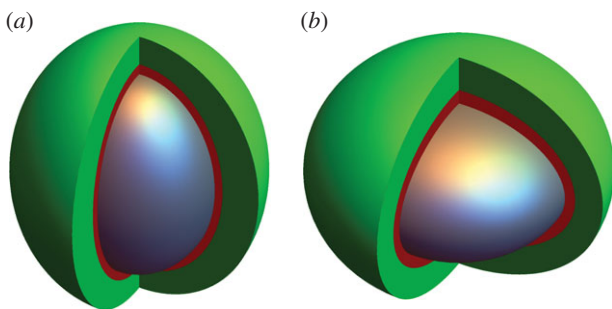

Figure 2. (*a*) Prolate spheroid and (*b*) oblate spheroid. The anoxic central core in both cases ($e = 0.75$) is depicted in grey, and the hypoxic extent in red, while well-oxygenated cells are shown in green. Both ellipsoids have the same volume necrotic core, but their resultant oxygen distributions are slightly different. See text for discussion.

oxygen partial pressure at the anoxic boundary must both be zero. For simple geometries such as perfectly spherical spheroids and cylindrical vessels, symmetry can be exploited to readily yield analytical solutions [33]. In elliptical geometry, the problem is more involved but the basic premise remains the same, and is outlined below. The geometry of the problem is illustrated in figure 3.

2.1. Prolate spheroids

In a prolate spherical geometry, we employ the prolate spherical coordinate system, using a geometrically intuitive definition where curves of constant σ are prolate spheroids, while curves of constant τ correspond to hyperboloids of revolution [34]. This is outlined in detail in the electronic supplementary material, text S1. This yields an analytical
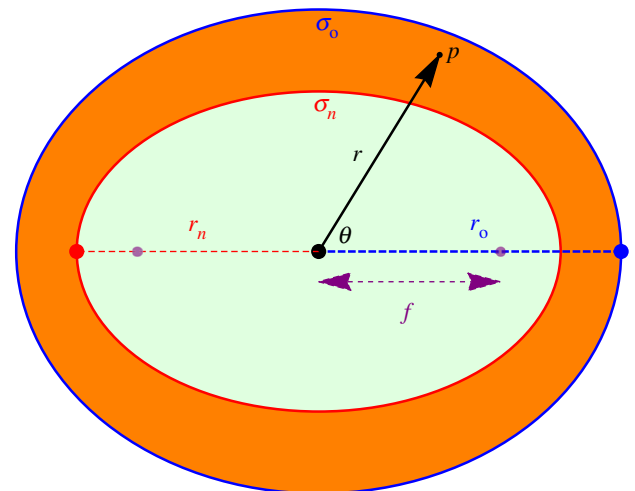

Figure 3. Geometry of a spheroid with outer semi-major axis length r_o and inner semi-major axis length r_n. On the surface σ_n, both partial pressure and oxygen flux are zero. On the outer surface $p(\sigma_o) = p_o$. In spherical coordinates, a point p is specified by a radial distance from centre r and an angle θ. The focal length of the inner spheroid is f.

solution, which can be converted directly into spherical coordinates to yield

$$P_P(r, \theta) = \frac{a\Omega}{6D}\left(r^2 - r_n^2 + f^2\sin^2\theta + f^2\log\left(\frac{r^2 - f^2\cos^2\theta}{r_n^2 - f^2}\right)\right.$$
$$\left. + \left(\frac{r_n^3}{f}\right)\log\left(\frac{(f + \sqrt{r^2 + f^2\sin^2\theta})(f - r_n)}{(f - \sqrt{r^2 + f^2\sin^2\theta})(f + r_n)}\right)\right),$$
$$(2.2)$$

where $f = er_n$ is the distance from the ellipse centre to the foci.

2.2. Oblate spheroids

In oblate spherical geometry, a similar geometrical definition exists [35] and can be solved through similar methods, also outlined in the electronic supplementary material, S1. The full solution in spherical coordinates is

$$P_O(r,\theta) = \frac{a\Omega}{6D}\left(r^2 - r_n^2 + f^2\sin^2\theta + 2f^2\log\left(\frac{r^2 + f^2\sin^2\theta}{r_n^2}\right)\right.$$
$$+ \frac{2(r_n^2 + 2f^2)(\sqrt{r_n^2 - f^2})}{f}\left(\arctan\left(\frac{f}{\sqrt{r^2 - f^2\cos^2\theta}}\right)\right.$$
$$\left.\left. - \arctan\left(\frac{f}{\sqrt{r_n^2 - f^2}}\right)\right)\right). \tag{2.3}$$

Both the prolate and oblate form can be alternatively cast in terms of r_o, the outer semi-major axis length, if preferable. These forms are also given in the electronic supplementary material, S1.

2.3. Ellipsoidal confocality

Analogous to the perfect spherical case, confocal elliptical surfaces in a spheroid are at the same oxygen partial pressure. For confocal ellipsoidal shells, focal length is constant, related to the eccentricity e_c and semi-major axis of the shell r_c by

$$f = e_c r_c. \tag{2.4}$$

It follows that the innermost (anoxic) and outermost ellipsoidal shells are confocal, thus for a true spheroid $e_o r_o = e_n r_n$. Within the bounds of acceptable experimental error, this relationship can be used to determine whether a given spheroid displaying apparent eccentricity is ellipsoidal or not. This is important from an experimental perspective, as sectioning can introduce serious distortions in fixed spheroid sections, or can miss the central axis of the spheroid [32]. In these cases, an ostensible ellipsoidal shape might be observed, but may in fact be a sectioning distortion or off-centre cut. Testing for confocality thus determines the underlying reality.

2.4. OCR estimation in spheroids

In the perfectly spherical case, OCR (in mmHg s^{-1}) is related to the anxoic radius r_n and outer radius r_o [28,32] by

$$a\Omega = \frac{6Dp_o}{r_o^2 + 2r_n^3/r_o - 3r_n^2}. \tag{2.5}$$

For a prolate tumour spheroid, it is possible to estimate OCR in a manner analogous to the spherical case by re-arranging the equations for P_P to yield

$$a\Omega = 6Dp_o\left(r_o^2 - r_n^2 + f^2\log\left(\frac{r_o^2 - f^2}{r_n^2 - f^2}\right) + \left(\frac{r_n^3}{f}\right)\log\left(\frac{(f + r_o)(f - r_n)}{(f - r_o)(f + r_n)}\right)\right)^{-1}. \tag{2.6}$$

Similarly for oblate spheroids, OCR is given by re-arrangement of P_O to arrive at

$$a\Omega = 6Dp_o\left(r_o^2 - r_n^2 + 4f^2\log\left(\frac{r_o}{r_n}\right)\right.$$
$$\left. + \frac{2(r_n^2 + 2f^2)(\sqrt{r_n^2 - f^2})}{f}\left(\arctan\left(\frac{f}{\sqrt{r_o^2 - f^2}}\right) - \arctan\left(\frac{f}{\sqrt{r_n^2 - f^2}}\right)\right)\right)^{-1}. \tag{2.7}$$

One complication that may arise is that it may be impossible to ascertain whether an ellipsoidal spheroid is prolate or oblate. In that case, one can produce a 'combined' expression for average OCR by taking the average of equations (2.2) and (2.3) and re-arranging to arrive at

$$a\Omega = 6Dp_o\left(r_o^2 - r_n^2 + f^2\log\left(\frac{r_o^2\sqrt{r_o^2 - f^2}}{r_n^2\sqrt{r_n^2 - f^2}}\right) + \frac{r_n^3}{2f}\log\left(\frac{(f + r_o)(f - r_n)}{(f - r_o)(f + r_n)}\right)\right.$$
$$\left. + \frac{(r_n^2 + 2f^2)(\sqrt{r_n^2 - f^2})}{f}\left(\arctan\left(\frac{f}{\sqrt{r_o^2 - f^2}}\right) - \arctan\left(\frac{f}{\sqrt{r_n^2 - f^2}}\right)\right)\right)^{-1}. \tag{2.8}$$

An example of the implementation of these forms including error analysis is included in the code given in electronic supplementary material, S2.

2.5. Spherical error metrics

It is worthwhile introducing metrics to quantify how divergent the estimated oxygen profile in a given ellipsoidal spheroid is from a related perfectly symmetric spheroid. A perfect spheroid has radial symmetry, and thus $P(r_o) = p_o$ at all points. Consider related prolate and oblate spheroids with both semi-major axis r_o and eccentricity e, nested inside a sphere of radius r_o. We can define the root mean square error (RMSE) by contrasting the expected outer shell partial pressure p_o with what would be measured for spheroids at $P_P(r_o, \theta)$ and $P_O(r_o, \theta)$, respectively. The RMSE for prolate and oblate spheroids, respectively, is

$$\text{RMSE}_P = \sqrt{\frac{1}{2\pi}\int_0^{2\pi}(P_P(r_o,\theta) - p_o)^2\,d\theta} \tag{2.9}$$

and

$$\text{RMSE}_O = \sqrt{\frac{1}{2\pi}\int_0^{2\pi}(P_O(r_o,\theta) - p_o)^2\,d\theta}. \tag{2.10}$$

These equations can readily be solved by numerical integration methods, and solutions are demonstrated in the electronic supplementary material, code S2. Percentage error is simply $100(\text{RMSE}/p_o)$, and thus the variation in RMSE with eccentricity can be readily calculated. The other instance when deviation from spherical assumptions must be quantified is in OCR calculation; for example, when the OCR in a spheroid is calculated assuming the perfectly spherical form in equation (2.5) rather than a more appropriate prolate or oblate form. This might occur when eccentricity is low and the spheroid appears to be entirely symmetric to a first approximation. The distance from the centroid of a spheroid with semi-major axis r and focal length f to a point on the spheroid at an angle θ is given by $r\sqrt{1 - e^2\sin^2\theta}$, and thus the average values for outer radius r_o and anoxic radius r_n are given by integrating this over a full revolution, yielding

$$\langle r_o\rangle = \frac{2r_o}{\pi}E_m\left(\frac{f^2}{r_o^2}\right) \tag{2.11}$$

and

$$\langle r_n\rangle = \frac{2r_n}{\pi}E_m\left(\frac{f^2}{r_n^2}\right), \tag{2.12}$$

where E_m is the complete elliptic integral of the second kind. Analogous to the discrete standard deviation, the distance function can be integrated over a full rotation $(\Delta r = \sqrt{(1/2\pi)\int_0^{2\pi}(r\sqrt{1 - e^2\sin^2\theta} - \langle r\rangle)^2 d\theta})$ to yield an

expression for standard deviation across these spheroids of

$$\Delta r_{\mathrm{o}} = r_{\mathrm{o}}\sqrt{\left(1 - \frac{f^2}{2r_{\mathrm{o}}^2}\right) - \frac{4}{\pi^2}E_m^2\left(\frac{f^2}{r_{\mathrm{o}}^2}\right)}$$
$$= \sqrt{r_{\mathrm{o}}^2 - \frac{f^2}{2} - \langle r_{\mathrm{o}}\rangle^2} \qquad (2.13)$$

and

$$\Delta r_n = r_n\sqrt{\left(1 - \frac{f^2}{2r_n^2}\right) - \frac{4}{\pi^2}E_m^2\left(\frac{f^2}{r_n^2}\right)}$$
$$= \sqrt{r_n^2 - \frac{f^2}{2} - \langle r_n\rangle^2}. \qquad (2.14)$$

Applying the form in equation (2.5) for spherical OCR yields an approximation (which is incorrect when $e > 0$) of

$$a\Omega_W = \frac{6Dp_{\mathrm{o}}\langle r_{\mathrm{o}}\rangle}{\langle r_{\mathrm{o}}\rangle^3 + 2\langle r_n\rangle^3 - 3\langle r_{\mathrm{o}}\rangle\langle r_n\rangle^2}. \qquad (2.15)$$

The uncertainty calculation associated with this can be calculated with the variance formula, in this case given by

$$\Delta a\Omega_W = \sqrt{\left(\frac{\partial(a\Omega)}{\partial r_{\mathrm{o}}}\right)^2\Delta r_{\mathrm{o}}^2 + \left(\frac{\partial(a\Omega)}{\partial r_n}\right)^2\Delta r_n^2}. \qquad (2.16)$$

This is analytically tractable, and is given in the electronic supplementary material, S1. An implementation in several code languages is also provided in the electronic supplementary material, S2.

3. Methods

3.1. Spheroid oxygen profiles
The models derived in this work were used to create oxygen profiles for spheroids of both prolate and oblate classes, which were contrasted to conventional perfectly spherical profiles.

3.2. Quantifying differences between prolate and oblate cases
Prolate and oblate forms have some mathematical differences, as can be seen by inspection of equations (2.2) and (2.3). Whether this difference is experimentally significant is an important question; from a single projection of a tumour spheroid it might be impossible to ascertain whether an experimenter is dealing with a prolate or oblate case. As an experimentalist might not be able to determine whether a given spheroid is prolate or oblate from a single section, quantifying differences in measured OCR under each assumption is an important goal of this work. This was simulated by producing prolate and oblate spheroids with properties as outlined in table 1, and observing the differences in their profiles. In addition, OCR estimates under the 'wrong' assumptions were also calculated and inspected. Specifically, the 'wrong' assumption occurs when one applies oblate equations for a prolate spheroid or vice versa. OCR was also calculated with the combined assumption (equation (2.8)), which can also be used when the underlying form is unknown. These spheroids were produced with physical properties as per table 1, with OCR given by equations (2.5)–(2.8).

3.3. Comparisons with the spherical case
As OCR from spheroids is estimated assuming spherical symmetry, a major aspect of this work was quantifying precisely how close to perfect sphericity spheroids must be so that such

Table 1. Simulation parameters.

parameter	simulation value
semi-major axis	500 μm
oxygen consumption rate (a)	20 mmHg s^{-1}
external partial pressure (p_{o})	100 mmHg

an assumption holds, and how departures from sphericity impact estimates of OCR and oxygen profiles. To study this, spheroids with known OCR and varying eccentricity were simulated, and analysed with equations (2.9)–(2.16).

3.4. Experimental proof of concept
To date, non-spherical tumour spheroids have been somewhat neglected, and have been frequently discarded from analysis due to their inherent uncertainty. It is thus difficult to find non-spherical tumour spheroid data. A potential example was taken from a previously analysed set of sectioned DLD-1 tumour spheroids [32], dual-stained with proliferation marker Ki-67 and EF5. Spheroids from this set were experimentally determined to have an OCR of 22.10 ± 4.24 mmHg s^{-1}. The sample spheroid was excluded from prior analysis because of its high eccentricity (external eccentricity $e \approx 0.66$). This was then analysed using methods outlined in this work as a proof of concept to determine OCR, contrasting it with known values and spherical estimates.

4. Results

4.1. Oxygen distributions in spheroids
Eccentric spheroids were simulated with properties shown in table 1. Unlike the spherical case, oxygen profiles here are not radially symmetric, so profiles were plotted along both the semi-major and semi-minor axis for clarity. Examples of these profiles are depicted in figure 4. Oxygen gradients through spheroids are simulated in figure 5, for both prolate and oblate cases with increasing eccentricity.

4.2. Quantification of differences in prolate and oblate spheroids
From two-dimensional sectioning or imagining alone, it can be experimentally difficult to ascertain whether a given spheroid is either prolate or oblate. It is thus important to quantify differences between the ellipsoids. Figures 4 and 5 suggest that prolate and oblate spheroids have broadly similar oxygen profiles until eccentricity approaches unity. Figure 6 depicts internal anoxic radii with eccentricity. These differ only slightly, typically less than or equal to 1% for both major and minor axes for $0 < e < 0.9$. More interesting perhaps is the variation in OCR estimate with eccentricity under the 'wrong' assumption (namely assuming oblate form when the actual entity is prolate or vice versa) shown in figure 7. This suggests strongly that OCR estimates arrived at under the 'wrong' assumption are still accurate up until high eccentricity. Even at very high eccentricity, an average value of both incorrect OCRs was extremely close to true OCR. This suggests that incorrectly specifying the type of spheroid should not greatly impact OCR estimates. For improved accuracy, employing the combined estimate in
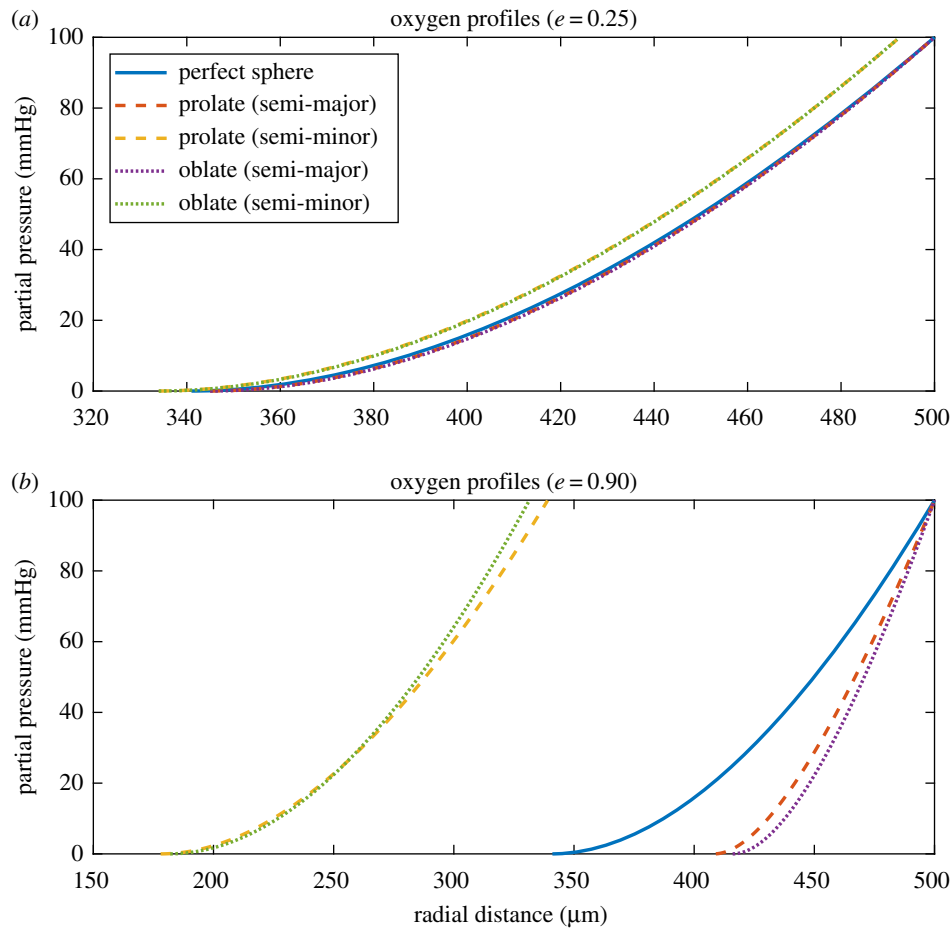
Figure 4. Oxygen profiles for both prolate and oblate spheroids along the semi-major and semi-minor axis for (a) a spheroid with inner eccentricity $e = 0.25$. There is relatively little difference between prolate and oblate cases and profiles largely overlap, being close to the spherical case. (b) A spheroid with inner eccentricity $e = 0.90$. Small differences between prolate and oblate cases can be readily seen, and a very large divergence from the perfectly spherical case is apparent. (Online version in colour.)

equation (2.8) yields even smaller errors, suggesting this could readily be used by experimentalists without introducing major error even when the underlying form is unknown.

4.3. Comparisons with spherical case

Table 2 depicts the impact of assuming perfect sphericity on derived OCR estimates for properties in table 1. At low e (typically $e \leq 0.3$), treating spheroids as perfect spheres yields acceptable accuracy for both OCR estimates. However, as $e \to 1$, the reliability of OCR estimates rapidly breaks down, and errors become increasingly large and unreliable.

4.4. Experimental proof of concept

For this work, a simple image analysis algorithm was written for the spheroid image, which found the ellipsoid centre and cast best fit ellipses from this position. The analysis algorithm was broadly similar to previously described methods [32], yielding estimates of $e \approx 0.66$, $r_o = 488.5\,\mu m$ and $r_n = 400.15\,\mu m$. This analysis suggested the best-fit inner and outer ellipses were approximately confocal to within experimental error, as required by the confocality condition in equation (2.4) ($e_o r_o \approx e_n r_n$ to within an error of 1.13%). Uncertainty on the lengths of $r_o\ r_n$ were taken from this to be $5.53\,\mu m$ and $4.52\,\mu m$, respectively. Results of this analysis are depicted in figure 8 and table 3, and suggest values in agreement with those previously measured when

considered as a prolate/oblate spheroid, and unrealistic values if presumed perfectly spherical.

5. Discussion

Analysis of spheroids to date tends to pivot on the presumption of sphericity, as symmetry arguments reduce the complexity required. However, real spheroids tend to depart from perfect sphericity to varying extents. In this work, we provide a metric for determining how reliable the simpler spherical assumption will be as eccentricity increases, as outlined in table 2. The methods outlined in this work can be employed to generate reliable estimates of OCR and oxygen distribution. Another major benefit of this work is that it allows an experimenter to determine OCR even in non-spherical cases when high eccentricity might otherwise render the spheroids in question ill-suited for analysis. Provided the inner and outer ellipses are suitably confocal, the analysis outlined in this work can be employed, and thus should help increase experimental throughput.

As depicted in table 2, presuming sphericity with eccentric sections yields acceptable accuracy when eccentricity is small, but rapidly begins to produce completely unrealistic results for OCR and massive uncertainty. When analysed as either prolate or oblate spheroids, however, OCR estimates are in agreement with the previously measured values. This suggests strongly that, for eccentricity
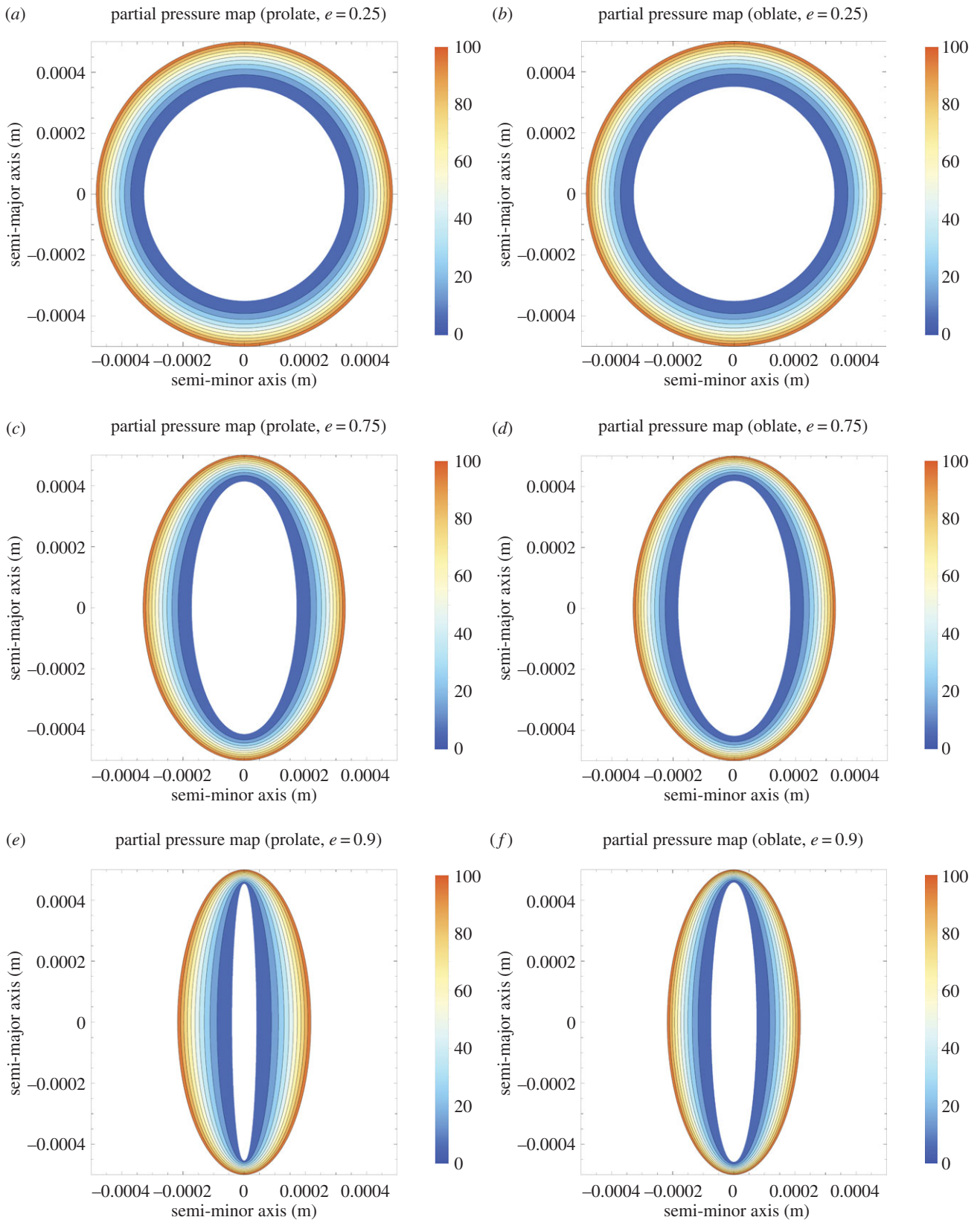
Figure 5. $(a-f)$ Contour oxygen maps for prolate and oblate spheroids with increasing eccentricity with semi-major axis 500 μm and OCR of 20 mmHg s^{-1}. Prolate and oblate have broadly similar oxygen maps, with divergence manifesting as $e \to 1$.

greater than approximately $e = 0.3$, spherical assumptions for OCR cease to be appropriate and ellipsoidal analysis must be employed. While data for this are currently sparse, we were able to demonstrate the principle on the highly eccentric spheroid illustrated in figure 8, determined by image analysis to have $f = 318.89 \pm 2.57$ μm. When analysed as a spheroid, OCR estimates were completely unrealistic with huge uncertainty, as seen in table 3. However, when considered as either

a prolate or oblate spheroid, OCR measurements were within previously measured values. This is promising, but, as only a single datum point is available, this should be interpreted solely as a proof of concept.

It is worth noting that, from single section images or microscopy, there is no obvious way to ascertain whether a spheroid is prolate or oblate. As the mathematical forms for these are slightly different, this adds an extra uncertainty
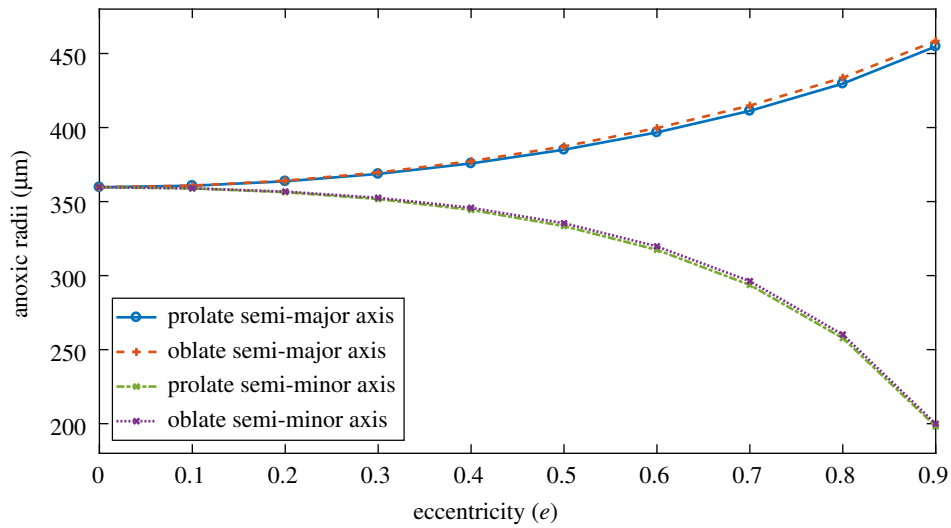
Figure 6. Variation of anoxic radii with eccentricity of outer shell from equations (2.2) and (2.3) for spheroids with properties as per table 2. Differences between radii in the prolate and oblate case are generally very small up to high eccentricity. (Online version in colour.)
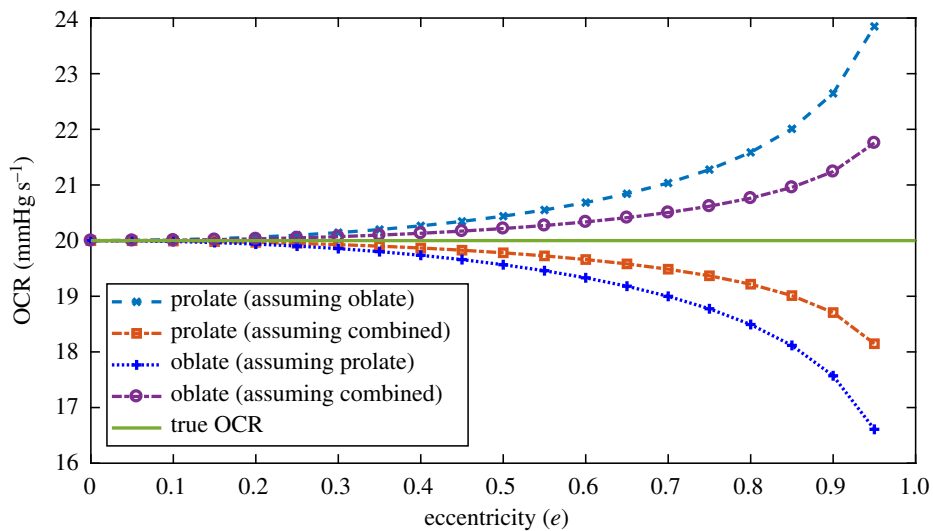

Figure 7. OCR estimates under 'wrong' assumptions for increasing inner eccentricity, calculated from equations (2.6)–(2.8). Combined OCR estimate yields smaller errors in all cases. True OCR is 20 mmHg s^{-1}. (Online version in colour.)

Table 2. RMSE and OCR estimates assuming sphericity for spheroids of varying eccentricity e.

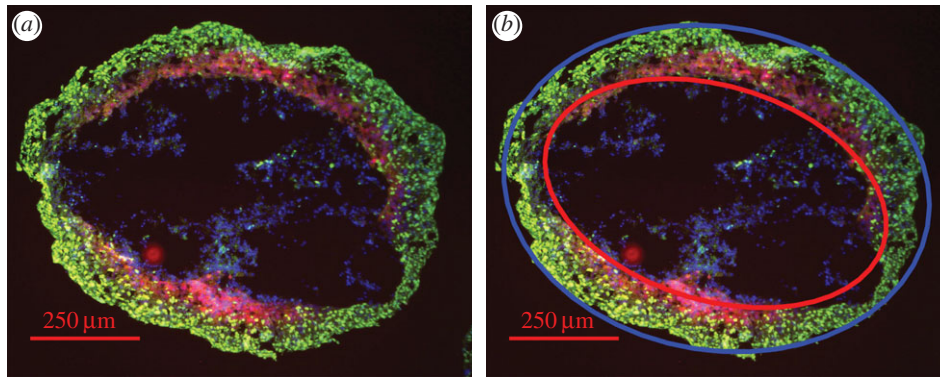| e	RMSE (prolate)	RMSE (oblate)	prolate OCR (mmHg s^{-1})	oblate OCR (mmHg s^{-1})
0	0%	0%	20.00 $\pm$ 0.00	20.00 $\pm$ 0.00
0.1	0.82%	0.82%	20.13 $\pm$ 0.37	20.14 $\pm$ 0.37
0.2	3.32%	3.33%	20.54 $\pm$ 1.53	20.60 $\pm$ 1.54
0.3	7.77%	7.78%	21.27 $\pm$ 3.73	21.42 $\pm$ 3.78
0.4	14.57%	14.60%	22.44 $\pm$ 7.47	22.75 $\pm$ 7.68
0.5	24.45%	24.55%	24.26 $\pm$ 13.91	24.84 $\pm$ 14.56
0.6	38.67%	38.94%	27.16 $\pm$ 25.76	28.25 $\pm$ 27.76
0.7	59.51%	60.17%	32.25 $\pm$ 51.07	34.41 $\pm$ 57.82
0.8	91.53%	93.12%	43.16 $\pm$ 124.77	48.58 $\pm$ 156.72
0.9	146.17%	150.33%	85.56 $\pm$ 660.92	120.52 $\pm$ 1291.81

Figure 8. (*a*) Eccentric DLD-1 spheroid (contrast enhanced for clarity). (*b*) Demonstration of analysis with a spheroid image analysis algorithm detecting best-fit ellipses (blue ellipse best fit to outer boundary, red to inner). Calculated focal lengths from both are checked for confocality from equation (2.4) and OCR estimated. See text for details.

Table 3. OCR estimates for sample spheroid.

assumption	estimated OCR (mmHg s^{-1})
previously measured for DLD-1 cell line	22.10 ± 4.24
assumption of perfect sphericity (true spheroid)	42.74 ± 51.98
assuming prolate tumour spheroid	29.25 ± 4.25
assuming oblate tumour spheroid	27.27 ± 4.11

Figure 9. The eccentricity of a sheared spheroid is the same for both anoxic and outer ellipsoids ($e = \sqrt{1 - 1/c^2}$) and thus not confocal as f is not constant. Sheared spheroids are not true spheroids, as the confocality condition is not met. (Online version in colour.)

and prompts the question about which form is preferable to employ. The analysis in this work (figures 6 and 7) indicates that, even if one incorrectly assumes the wrong form, OCR estimates are still very good, with only minimal errors introduced. This holds with only negligible errors until very high eccentricity. The combined OCR form in equation (2.8) yields only negligible error even when the underlying form is unknown. Thus, an experimenter should opt to use this form for OCR estimation when they have no other information on whether the specimen is prolate or oblate, as this does not introduce large errors even at high eccentricity.

While modelling of elliptical oxygen diffusion has the potential to greatly extend experimental throughput, there are a number of scenarios in which an ostensible eccentric spheroid might not be what it appears. For fixed and sectioned spheroids, the act of sectioning itself can be enough to induce substantial deformations, stretching it along a particular axis. Ostensibly, the resultant shape might appear ellipsoidal, but is in reality a warped spheroid, and cannot be reliably analysed with the methods outlined. Such an example is show in figure 9, for a spherical spheroid sheared along an axis. From the mathematics established in this work, we can distinguish between true spheroids and warped spheroids—if the inner and outer ellipses are not confocal ($e_o r_o \neq e_n r_n$) then the shape is a warped spheroid, and should be discounted from analysis, as per figure 1. Crucially, figure 9 demonstrates that warped spheroids can only satisfy the ellipsoidal confocality condition under two circumstances: either when its eccentricity is 0 (a perfect sphere), or the non-physical situation when $r_o = r_n$. Thus, a sheared spheroid in one direction will never come close to satisfying the ellipsoidal
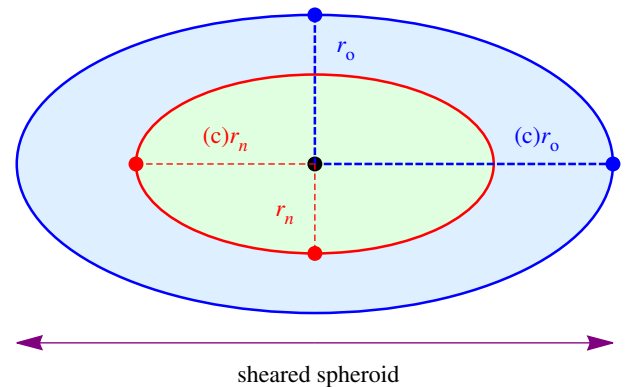
confocality condition. In practice, all experimental work comes with inherent uncertainty, so $e_o r_o \approx e_n r_n$ within the bounds of image analysis uncertainty is sufficient to determine whether a spheroid can be treated as an ellipsoidal case.

There is a more subtle issue with sectioned spheroids, which becomes even more crucial with sectioned eccentric spheroids. Analysis relies on a section through the central axis of the spheroid. In the perfectly spherical case, if the section is off-centre, the net result will be two concentric circles but with a misleading ratio, rendering any OCR calculation derived from this suspect. By contrast, any plane through an ellipsoid produces an ellipse, but if these cuts are off the central axis then the inner and outer ellipses will no longer have a common centre, and will not be confocal. In this regard, determining an off-centre ellipsoid section is relatively straight-forward. A proof of this is provided in the electronic supplementary material, S1.

The theoretical analysis outlined here presents biological investigators with new methods for extending spheroid analysis, and the means to interpret data which depart from sphericity. It also establishes uncertainty bounds on existing spherical analysis techniques, and methods for determining OCR and oxygen distribution in tumour ellipsoids. The findings of this work will increase experimental confidence with tumour spheroids, and have the potential to substantially increase experimental throughput, improving our insights on everything from tumour hypoxia to drug delivery. Such an approach is imperative if we are to fully exploit this unique

experimental tool, and ultimately marshal the new insights obtained towards better cancer treatment and diagnostics.

References

1. Grimes DR, Partridge M. 2015 A mechanistic investigation of the oxygen fixation hypothesis and oxygen enhancement ratio. *Biomed. Phys. Eng. Express* **1**, 45209. (doi:10.1088/2057-1976/1/4/045209)

2. Hall EJ, Giaccia AJ. 2006 *Radiobiology for the radiologist*, vol. 6. Philadelphia, PA: Lippincott Williams & Wilkins.

3. Wenzl T, Wilkens JJ. 2011 Modelling of the oxygen enhancement ratio for ion beam radiation therapy. *Phys. Med. Biol.* **56**, 3251–3268. (doi:10.1088/0031-9155/56/11/006)

4. Grimes DR, Warren DR, Partridge M. 2017 An approximate analytical solution of the Bethe equation for charged particles in the radiotherapeutic energy range. *Sci. Rep.* **7**, 9781. (doi:10.1038/s41598-017-10554-0)

5. Bentzen SM, Gregoire V. 2011 Molecular imaging-based dose painting: a novel paradigm for radiation therapy prescription. *Semin. Radiat. Oncol.* **21**, 101–110. (doi:10.1016/j.semradonc.2010.10.001)

6. Grimes DR, Warren DR, Warren S. 2017 Hypoxia imaging and radiotherapy: bridging the resolution gap. *Br. J. Radiol.* **90**, 20160939. (doi:10.1259/bjr.20160939)

7. Gray LH, Conger A, Ebert M, Hornsey S, Scott O. 1953 The concentration of oxygen dissolved in tissues at the time of irradiation as a factor in radiotherapy. *Br. J. Radiol.* **26**, 638–648. (doi:10.1259/0007-1285-26-312-638)

8. Vaupel P, Thews O, Hoeckel M. 2001 Treatment resistance of solid tumors. *Med. Oncol.* **18**, 243–259. (doi:10.1385/MO:18:4:243)

9. Vaupel P, Briest S, Höckel M. 2002 Hypoxia in breast cancer: pathogenesis, characterization and biological/therapeutic implications. *Wiener Medizinische Wochenschrift* **152**, 334–342. (doi:10.1046/j.1563-258X.2002.02032.x)

10. Vaupel P, Mayer A, Höckel M. 2004 Tumor hypoxia and malignant progression. In *Methods in enzymology* (eds JN Abelson, MI Simon), vol. 381, pp. 335–354. Amsterdam, The Netherlands: Elsevier.

11. Lu X, Kang Y. 2010 Hypoxia and hypoxia-inducible factors: master regulators of metastasis. *Clin. Cancer. Res.* **16**, 5928–5935. (doi:10.1158/1078-0432.CCR-10-1360)

12. Mujcic H, Hill R, Koritzinsky M, Wouters B. 2014 Hypoxia signaling and the metastatic phenotype. *Curr. Mol. Med.* **14**, 565–579.

13. Sullivan R, Graham CH. 2007 Hypoxia-driven selection of the metastatic phenotype. *Cancer Metastasis Rev.* **26**, 319–331. (doi:10.1007/s10555-007-9062-2)

14. Grimes DR, Kannan P, Warren DR, Markelc B, Bates R, Muschel R, Partridge M. 2016 Estimating oxygen distribution from vasculature in three-dimensional tumour tissue. *J. R. Soc. Interface* **13**, 20160070. (doi:10.1098/rsif.2016.0070)

15. Rankin EB, Nam JM, Giaccia AJ. 2016 Hypoxia: signaling the metastatic cascade. *Trends Cancer* **2**, 295–304. (doi:10.1016/j.trecan.2016.05.006)

16. Secomb TW, Hsu R, Park EY, Dewhirst MW. 2004 Green's function methods for analysis of oxygen delivery to tissue by microvascular networks. *Ann. Biomed. Eng.* **32**, 1519–1529.

17. Hirschhaeuser F, Menne H, Dittfeld C, West J, Mueller-Klieser W, Kunz-Schughart LA. 2010 Multicellular tumor spheroids: an underestimated tool is catching up again. *J. Biotechnol.* **148**, 3–15. (doi:10.1016/j.jbiotec.2010.01.012)

18. Gomes A, Guillaume L, Grimes DR, Fehrenbach J, Lobjois V, Ducommun B. 2016 Oxygen partial pressure is a rate-limiting parameter for cell proliferation in 3D spheroids grown in physioxic culture condition. *PLoS ONE* **11**, e0161239. (doi:10.1371/journal.pone.0161239)

19. Leek R, Grimes DR, Harris AL, McIntyre A. 2016 Methods: using three-dimensional culture (spheroids) as an *in vitro* model of tumour hypoxia. In *Tumor microenvironment* (eds C Koumenis, LM Coussens, A Giaccia, E Hammond), pp. 167–196. Berlin, Germany: Springer.

20. Santini M, Rainaldi G, Indovina P. 1999 Multicellular tumour spheroids in radiation biology. *Int. J. Radiat. Biol.* **75**, 787–799. (doi:10.1080/095530099139845)

21. Dubessy C, Merlin JL, Marchal C, Guillemin F. 2000 Spheroids in radiobiology and photodynamic therapy. *Crit. Rev. Oncol. Hematol.* **36**, 179–192. (doi:10.1016/S1040-8428(00)00085-8)

22. Madsen SJ, Sun CH, Tromberg BJ, Cristini V, De Magalh aes N, Hirschberg H. 2006 Multicell tumor spheroids in photodynamic therapy. *Lasers Surg. Med.* **38**, 555–564. (doi:10.1002/lsm.20350)

23. Kempf H, Bleicher M, Meyer-Hermann M. 2010 Spatio-temporal cell dynamics in tumour spheroid irradiation. *Eur. Phys. J. D* **60**, 177–193. (doi:10.1140/epjd/e2010-00178-4)

24. Dufau I, Frongia C, Sicard F, Dedieu L, Cordelier P, Ausseil F, Ducommun B, Valette A. 2012 Multicellular tumor spheroid model to evaluate spatio-temporal dynamics effect of chemotherapeutics: application to the gemcitabine/

CHK1 inhibitor combination in pancreatic cancer. *BMC Cancer* **12**, 15. (doi:10.1186/1471-2407-12-15)

25. Mehta G, Hsiao AY, Ingram M, Luker GD, Takayama S. 2012 Opportunities and challenges for use of tumor spheroids as models to test drug delivery and efficacy. *J. Control. Release* **164**, 192–204. (doi:10.1016/j.jconrel.2012.04.045)

26. Kim TH, Mount CW, Gombotz WR, Pun SH. 2010 The delivery of doxorubicin to 3-D multicellular spheroids and tumors in a murine xenograft model using tumor-penetrating triblock polymeric micelles. *Biomaterials* **31**, 7386–7397. (doi:10.1016/j.biomaterials.2010.06.004)

27. Vinci M et al. 2012 Advances in establishment and analysis of three-dimensional tumor spheroid-based functional assays for target validation and drug evaluation. *BMC Biol.* **10**, 29. (doi:10.1186/1741-7007-10-29)

28. Grimes DR, Kannan P, McIntyre A, Kavanagh A, Siddiky A, Wigfield S, Harris A, Partridge M. 2016 The role of oxygen in avascular tumor growth. *PLoS ONE* **11**, e0153692. (doi:10.1371/journal.pone.0153692)

29. Fang D et al. 2010 Expansion of CD133$^+$ colon cancer cultures retaining stem cell properties to enable cancer stem cell target discovery. *Br. J. Cancer* **102**, 1265–1275. (doi:10.1038/sj.bjc.6605610)

30. Kelly CJ, Hussien K, Muschel RJ. 2012 3D tumour spheroids as a model to assess the suitability of [18F] FDG-PET as an early indicator of response to PI3K inhibition. *Nucl. Med. Biol.* **39**, 986–992. (doi:10.1016/j.nucmedbio.2012.04.006)

31. Mueller-Klieser W. 1984 Method for the determination of oxygen consumption rates and diffusion coefficients in multicellular spheroids. *Biophys. J.* **46**, 343–348. (doi:10.1016/S0006-3495(84)84030-8)

32. Grimes DR, Kelly C, Bloch K, Partridge M. 2014 A method for estimating the oxygen consumption rate in multicellular tumour spheroids. *J. R. Soc. Interface* **11**, 20131124. (doi:10.1098/rsif.2013.1124)

33. Grimes DR, Fletcher AG, Partridge M. 2014 Oxygen consumption dynamics in steady-state tumour models. *R. Soc. open. sci.* **1**, 140080. (doi:10.1098/rsos.140080)

34. Prolate spheroidal coordinates (Wikipedia entry). 2018 See https://en.wikipedia.org/wiki/Prolate_spheroidal_coordinates.

35. Oblate spheroidal coordinates (Wikipedia entry). 2018 See https://en.wikipedia.org/wiki/Oblate_spheroidal_coordinates.